

Poster3-26 IMPACT OF THE RADAR DIFFERENTIAL PHASE UPON TRANSMISSION ON THE POLARIMETRIC VARIABLES

Valery Melnikov

CIMMS, University of Oklahoma and National Severe Storms Laboratory, Norman, OK.

valery.melnikov@noaa.gov

1. Introduction

The vast majority of polarimetric weather radars employs Simultaneous transmission of horizontally (H) and vertically (V) polarized electromagnetic waves (SHV radar design). The different lengths of the H and V signal paths in such radars cause differential phase ψ_t upon transmission and differential phase ψ_r upon reception. In calculations of the particles' scattering properties, these system phases are silently assumed to be zero. Polarization properties calculated under such an assumption can be measured with radars employing alternate transmission of polarized waves (AHV radar design). For SHV radars, the system phases must be taken into consideration and impacts of ψ_t on differential reflectivity (Z_{DR}), the backscatter differential phase (δ), and copolar correlation coefficient (ρ_{hv}) are observable (e.g., Melnikov 2018).

The system phases and the phase difference upon propagation contribute to the phases of incident radiation which should be considered in scattering problems. The phase of incident radiation consists of the system phase upon transmission and the phase shift due to propagation in a media. To show the system phase effects, the incident phase is considered here interchangeably with the system phase upon transmission.

Ice particles of pristine ice plates and columns in a shape of ellipsoids (e.g., Hall et al. 1984, Bader et al. 1987, Hogan et al. 2002, Westbrook et al. 2010) and hexagonal prisms (Westbrook 2014) as well as ice dendrites (e.g., Shrom and Kumjian 2018) are considered here. It is shown in the next section that maximal Z_{DR} and δ from ice particles can be quite different for SHV and AHV radars.

Polarization properties of melting ice particles are poorly understood. Experimental observations of ice particles in the melting layer (e.g., Fabry and Zawadzki 1995, Fabry and Szyrmer 1999, Szyrmer and Zawadzki 1999, Tromel et al. 2012, Griffin et al. 2018, 2019) have established large intervals of observed Z_{DR} , ρ_{hv} , and δ values, but a few publications contain interpretations of the measurements (e.g., Melnikov et al. 2005, Melnikov 2012, Tromel et al. 2013). Melnikov et al. (2005) and Melnikov (2012) considered Rayleigh particles and documented a few degrees of δ in the melting layer. Tromel et al (2013) attributed nonzero δ to resonant scattering effects. It is shown in section 3 that the Rayleigh scatterers can produce δ of several degrees.

Melnikov et al. (2014) observed different ρ_{hv} values from adjacent WSR-88D radars in hail areas of thunderstorms. This difference is analyzed in section 4 and it is shown there that this effect can be due to the differential phase of the incident waves.

2. Maximal Z_{DR} and δ of pristine ice particles

Pristine ice cloud crystals in forms of plates and columns can be approximated with spheroids or hexagonal prisms having the semi-axes a and b ($a \geq b$). Orientation of a scatterer is characterized with angles θ and φ (Fig. 1). Scattering geometry can be described using the scattering plane (e.g., Holt 1984, Vivekanandan et. al 1991, Ryzhkov and Zrnice 2007); here, the laboratory frame affixed to the ground is used (Fig. 1), which naturally describes orientations of cloud particles relative to the ground. In this frame, θ is the canting angle and the incident waves can be assumed horizontally and vertically polarized at low antenna elevation angles.

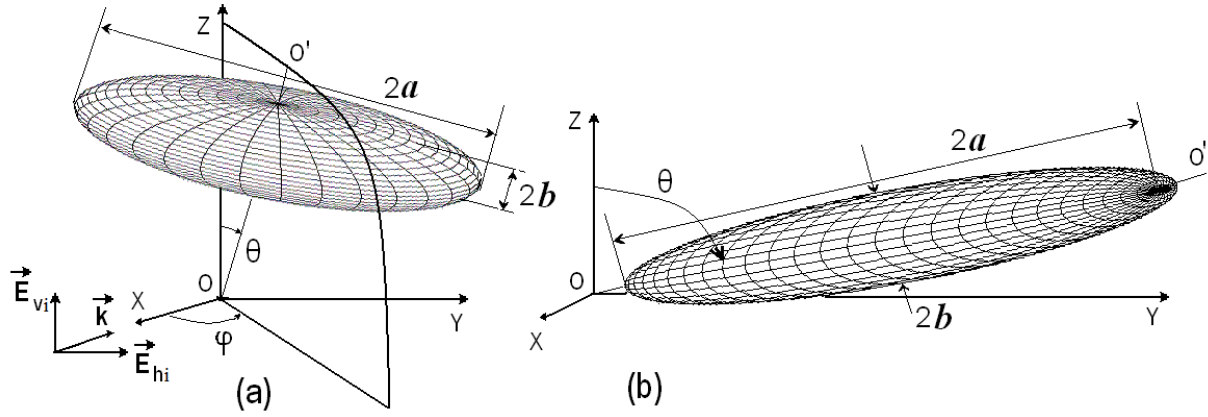


Fig. 1. Geometry of scattering by (a) plate-like and (b) columnar scatterers approximated with spheroids. E_{hi} and E_{vi} are the amplitudes of incident horizontally and vertically polarized waves propagating in direction \vec{k} .

The Z_{DR} and δ values from cloud particles depend on their shape, axis ratio (width/length), dielectric permittivity, and orientations relative to polarization planes of incident radiation. In the absence of strong electric fields, ice particles fall with their larger dimension being horizontal in the mean (Pruppacher and Klett, 1997, section 10). In thunderstorms, cloud ice particles can be strongly aligned (Hendry and McCormick 1976, Caylor and Chandrasekar 1996, Ryzhkov and Zrnice 2007, Hubert et al. 2014a,b) so they can have any orientation relative to the radar beam. Therefore, to analyze the polarization properties of ice particles in thunderstorms, the angles θ and φ can be considered to be fixed at any θ and φ in the intervals $0 \leq \theta \leq 180^\circ$ and $0 \leq \varphi \leq 360^\circ$.

SHV radar transmits two orthogonally polarized waves, which for low elevation angles can be called horizontally and vertically polarized ones. Due to differential phase upon propagation and ψ_t , the differential phase of incident (subscript i) waves is

$$\psi_i = \psi_t + \Phi_{DP}/2, \quad (1)$$

where Φ_{DP} is the two way propagation differential phase. Scattering of horizontally (subscript h) and vertically (subscript v) polarized electromagnetic waves is described by the scattering matrix S_{mn} (m and n are any of h and v). Let E_{hi} and E_{vi} be the amplitudes of the incident waves (Fig. 1); then the scattered (subscript s) waves E_{hs} and E_{vs} are written as,

$$\begin{pmatrix} E_{hs} \\ E_{vs} \end{pmatrix} = \begin{pmatrix} S_{hh} & S_{hv} \\ S_{hv} & S_{vv} \end{pmatrix} \begin{pmatrix} E_{hi} \\ E_{vi} e^{j\psi_i} \end{pmatrix}, \quad (2)$$

where j is imaginary unity. The latter equation is written in backscatter alignment, therefore, $S_{hv} = S_{vh}$.

SHV radar typically transmits waves of different amplitudes and phases because of differences in their paths and losses in radar. The receive gains in the polarization channels may be different as well. Corrections for the system amplitude imbalances are done in Z_{DR} calibration. After the calibration, the transmitted wave amplitudes can be considered equal, i.e., $E_{vi} = E_{hi} = E_h$, and the received waves can be represented as,

$$\begin{pmatrix} E_{hr} \\ E_{vr} \end{pmatrix} = C_R \begin{pmatrix} 1 & 0 \\ 0 & e^{j\psi_r + j\Phi_{DP}/2} \end{pmatrix} \begin{pmatrix} S_{hh} & S_{hv} \\ S_{hv} & S_{vv} \end{pmatrix} \begin{pmatrix} 1 & 0 \\ 0 & e^{j\psi_t + j\Phi_{DP}/2} \end{pmatrix} \begin{pmatrix} E_h \\ E_h \end{pmatrix}, \quad (3)$$

where C_R is the radar constant with range normalization included. The first and third matrixes on the right hand side of (3) describe propagation of the waves from radar to the resolution volume and back. C_R and the amplitude E_h will be omitted in the following discussion because Z_{DR} , ρ_{hv} , and δ are relative values. The zero off-diagonal terms in the propagation matrixes in (3) mean negligible depolarization in the propagation media in which differential attenuation is negligible. Eq. (3) can be written as,

$$E_{hr} = S_{hh} + S_{hv} e^{j\psi_i} \quad \text{and} \quad E_{vr} = (S_{vv} e^{j\psi_i} + S_{hv}) e^{j\psi_r + j\Phi_{DP}/2}. \quad (4)$$

The scattering matrix elements of a single particle can be represented as,

$$S_{hh} = \alpha_a + \Delta\alpha \sin^2\theta \sin^2\varphi, \quad S_{vv} = \alpha_a + \Delta\alpha \cos^2\theta, \quad S_{hv} = \Delta\alpha \sin\theta \cos\theta \sin\varphi,$$

$$\Delta\alpha = \alpha_b - \alpha_a, \quad (5)$$

where α_a and α_b are polarizabilities along the major particle's axes (α_a refers to the longer axis), [e.g., Brongi and Chandrasekar 2001, eq. (2.53)]. Substitution (5) into (4) yields

$$E_{hr} = \alpha_a + \Delta\alpha A \sin\theta \sin\varphi, \quad (6)$$

$$E_{vr} = (\alpha_a e^{j\psi_i} + \Delta\alpha A \cos\theta) e^{j\psi_r + j\Phi_{DP}/2} \quad (7)$$

with $A = \sin\theta \sin\varphi + \cos\theta e^{j\psi_i}$.

Z_{DR} and δ from a single scatterer (or a collection of scatterers equally oriented) are

$$Z_{DR} = 10 \log(|E_{hr}|^2 / |E_{vr}|^2) \quad \text{and} \quad (8)$$

$$\delta = \arg(E_{hr}^* E_{vr}) - \psi_t - \psi_i - \Phi_{DP}, \quad (9)$$

where $*$ stands for complex conjugate. The first addend on the right hand side of (9) is the total measured differential phase. To obtain δ , we have to subtract the propagation and system differential phases from the total phase. One can see from (6)-(9) that measured Z_{DR} and δ depend on the axis ratio, orientation of the scatterer, and the system and propagation differential phases.

It is seen from (4) that the scattered waves have two contributions: the primary ones containing S_{hh} and S_{vv} and depolarized ones depending on S_{hv} . These mixed contributions are sometimes referred to as wave coupling upon scattering. Due to the coupling, Z_{DR} and δ values measured with SHV radar can significantly deviate from those measured with AHV radar. For AHV radar, (2) can also be used by setting

$S_{hv} = 0$ and $\psi_t = 0$. For such radar, the amplitudes of received waves are $E_{hr}^a = S_{hh}$ and $E_{vr}^a = S_{vv}$ (superscript a indicates alternate polarizations), i.e.,

$$E_{hr}^a = \alpha_a + \Delta\alpha \sin^2\theta \sin^2\varphi \quad \text{and} \quad E_{vr}^a = \alpha_a + \Delta\alpha \cos^2\theta. \quad (10)$$

For plates, $\Delta\alpha < 0$ and the maximal Z_{DR}^a and δ^a are attained at $\theta = 0$, i.e., at horizontal orientation of the scatterer:

$$Z_{DR}^a = 10\log(|\alpha_a|^2/|\alpha_b|^2) \quad \text{and} \quad \delta_{\max}^a = \arg(\alpha_a^* \alpha_b). \quad (11)$$

For a columnar scatterer, the maximal Z_{DR}^a and δ^a are attained at $\theta = \varphi = 90^\circ$, i.e., at its horizontal orientation of the particle (Fig 1b). For scatterers which are much smaller than the radar wavelength, i.e., in the Rayleigh scattering limit, polarizabilities $\alpha_{a,b}$ are (e.g., Doviak and Zrnicek 2006, section 8.5.2.4)

$$\alpha_{a,b} = V \frac{\varepsilon - 1}{1 + L_{a,b}(\varepsilon - 1)}, \quad (12)$$

where V is the scatterer's volume, ε is dielectric permittivity of ice ($\varepsilon = 3.17 - 0.0015j$ at S frequency band), and $L_{a,b}$ are the shape factors. The maximal Z_{DR} is attained for a very thin plate with $L_a = 0$ and $L_b = 1$, so (Gossard and Strauch 1983, Hogan et al. 2002)

$$Z_{DR\max}^a = 20\log(|\varepsilon|) = 10 \text{ dB}. \quad (13)$$

This value varies insignificantly at cm wavelengths. For thin long needles, $L_a = 0$ and $L_b = 0.5$, therefore

$$Z_{DR\max}^a = 20\log(|\varepsilon + 1|/2) = 6.4 \text{ dB}. \quad (14)$$

To obtain maximal Z_{DR} for thin needles randomly oriented on the horizontal plane, one has to average $|E_{hr}^a|^2$ and $|E_{vr}^a|^2$ from (10) over the angle φ at $\theta = 90^\circ$. The imaginary part of ε is very small compared to its real part and can be neglected, so (Hogan et al. 2002),

$$Z_{DR\max}^a = 10\log[1 + (|\varepsilon| - 1)/2 + 3(|\varepsilon| - 1)^2/32] = 4.0 \text{ dB}. \quad (15)$$

The phase δ_{\max}^a is calculated from the second equation in (11). For ice plates, $\delta_{\max}^a = -\arg(\varepsilon) = 0.03^\circ$ and for needles, $\delta_{\max}^a = -\arg(\varepsilon + 1) = 0.02^\circ$, i.e., very small values. Thus the differential phase upon backscattering by ice particles is negligible for AHV radar. Some cloud ice particles are better represented with a hexagonal prism (Westbrook 2014). Values of $\alpha_{a,b}$ are very close for very thin prisms and ellipsoids so the maximal Z_{DR} and δ for these shapes are equal.

Now, consider Z_{DR} and δ measured with SHV radar. Fig. 2 presents Z_{DR} as a function of θ ($0 - 180^\circ$) and φ ($0 - 360^\circ$) at $\psi_i = 0, 45,$ and 90° (ψ_i equals ψ_t in the figure). The values θ_{\max} and φ_{\max} are angles at which Z_{DR} attains its maximum. One can see that maximal Z_{DR} depends on ψ_i .

$Z_{DR} = 12.3 \text{ dB}$ is maximum maximum and attains at $\psi_t = 0$ or 180° , $\theta = 16^\circ$ or 106° , and $\varphi = 90^\circ$ or 270° ; a tilt in θ increases Z_{DR} over 10 dB obtained for AHV radar.

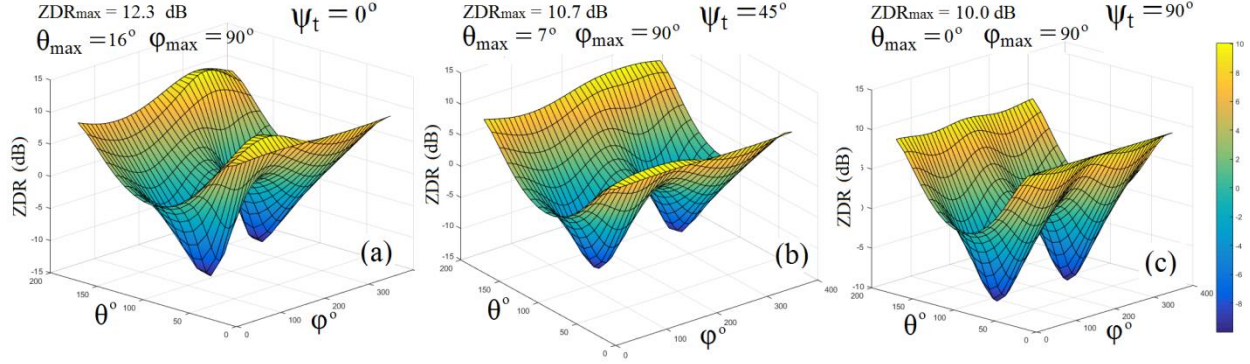


Fig. 2. Z_{DR} as a function of the angles θ and φ at (a) $\psi_t = 0^\circ$, (b) $\psi_t = 45^\circ$, and (c) $\psi_t = 90^\circ$ for pristine ice plates. $\psi_t = \psi_i$. The maximal Z_{DR} values at a given ψ_t along with the corresponding angles are shown at the tops of panels.

Z_{DR} as a function of θ and φ for ice needles are shown in Fig. 3. For these particles, the maximum maximum is 6.9 dB and is attained at $\theta = 10^\circ$, 170° , and $\psi_t = 0^\circ$. Maximal Z_{DR} does not depend on ψ_t significantly.

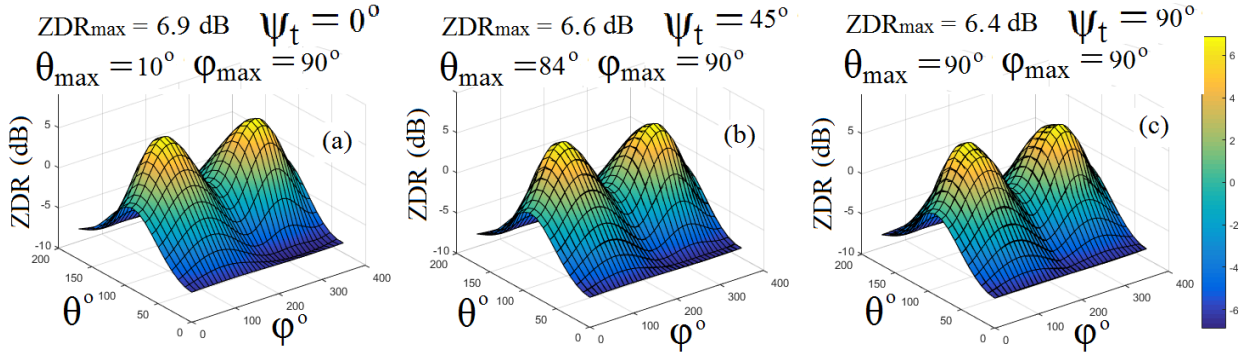


Fig. 3. Same as in Fig. 2, but for ice columns.

The phase $\bar{\delta}$ exhibits a strong dependence on ψ_t . Fig. 4 shows $\bar{\delta}$ as a function of θ and φ at $\psi_t = 90^\circ$. At $\psi_t = 0^\circ$, $\bar{\delta}$ is negligible for all θ and φ . The maximum maximum is $\bar{\delta}_{max} = 62.3^\circ$ attained at $\theta = 50^\circ$, $\varphi = 90^\circ$, and $\psi_t = 60^\circ$ for ice plates. For ice needles, the maximum maximum is $\bar{\delta}_{max} = 40.9^\circ$ attained at $\theta = 50^\circ$, $\varphi = 90^\circ$, and $\psi_t = 70^\circ$. These results for maximal Z_{DR} and $\bar{\delta}$ illustrate strong impacts of depolarized waves on the radar variables measured with SHV radar and this impact depends on the phase of incident radiation.

The values of $\bar{\delta}_{max}$ are large for thin ice particles (Fig. 4a) and can be positive and negative depending on ψ_i and orientation of the scatterers. This is in contrast to very small $\bar{\delta}$ values at alternate polarizations. The differential phase ψ_i depends upon the radar phase in transmit ψ_t , so to interpret the differential phases measured with a SHV radar, phase ψ_t should be known. The propagation differential phase Φ_{DP} , i.e., the second contributor to ψ_i , is routinely measured.

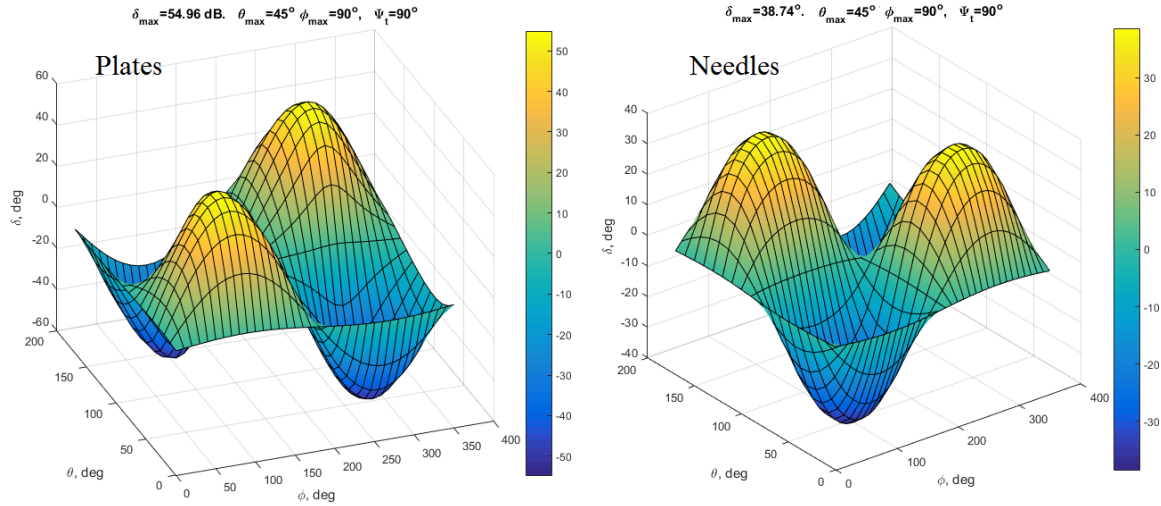


Fig. 4. Differential phase δ as a function of θ and φ at $\psi_i = 90^\circ$ (left) for ice plates and (right) ice columns.

Z_{DR} and δ can be positive and negative depending on orientations of scatterers and a value of ψ_i . Positive and negative Z_{DR} values are symmetrical relative to $Z_{DR} = 0$ dB. Positive maximum maximum Z_{DR} values are shown in Fig. 5a as a function of ψ_i . Negative Z_{DR} curves (not shown) can be obtained by rotating the positive curves about $Z_{DR} = 0$ dB axis. Values of maximum maximum δ exhibit different symmetry (Fig. 5b). Negative δ of -6° .. -8° have been observed in radar echoes from smoke plumes containing columnar scatterers (Melnikov et al. 2008, 2009).

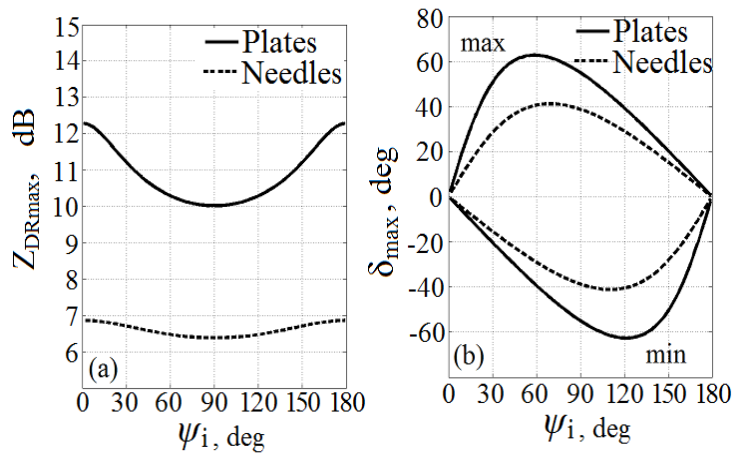


Fig. 5.(a): Maximum maximum $Z_{DR_{max}}$ and (b) δ_{max} as functions of the incident differential phase for thin ice plates (solid curves) and ice columns (dash curves). The negative δ values are marked with “min” in panel (b). SHV radar.

Hexagonal prisms are a better representation for pristine ice plates (Fig. 6a). The previous results are valid for very thin ellipsoids and hexagonal prisms, i.e., at $b/a \ll 1$. Maximal Z_{DR} and δ for a moderate b/a exhibit dependences on the particle’s habit. The maximum maximum $Z_{DR_{max}}$ values for ellipsoids are about 1 dB larger than those for prisms at a moderate $b/a = 0.3$ (Fig. 6a). The values of δ_{max} are

noticeably different for prisms and ellipsoids (Fig. 6a). The polarization properties of hexagonal prisms have been obtained with the WIPL-D software, which uses the method of moments to correctly solve scattering problems of bodies of arbitrary shapes and dielectric compositions (<https://wipl-d.com/>).

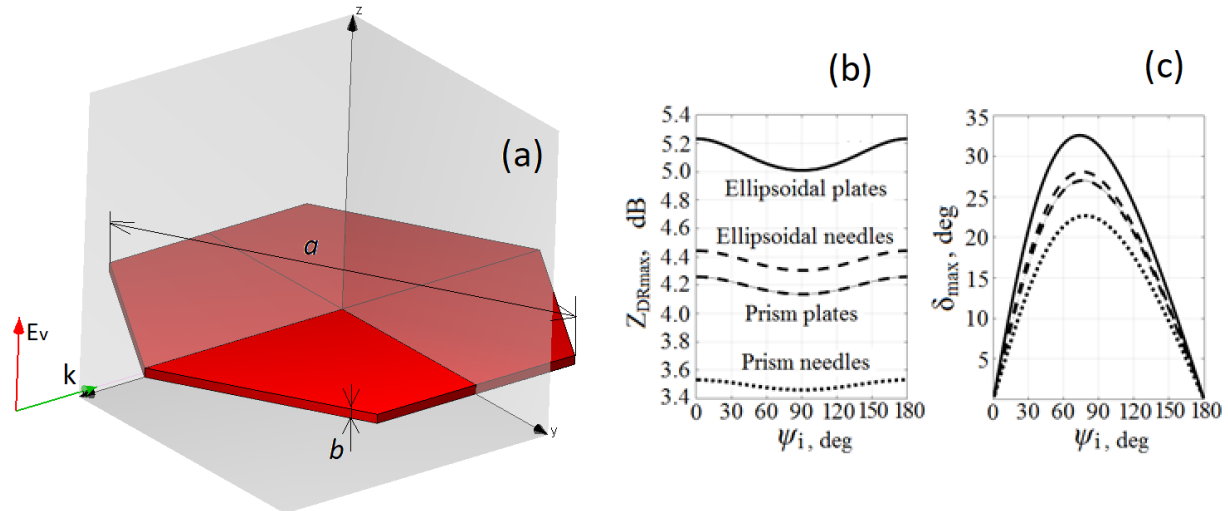


Fig. 6. (a): Thin hexagonal ice prism having the dimensions a and b ; also shown is the amplitude of vertically polarized incident wave. (b) and (c): Same as in Fig. 5, but for $b/a = 0.3$ and for ellipsoids and prisms. The legend in panel (b) is applicable for curves in panel (c).

Positive and negative δ are frequently observed in thunderstorms. One can see an increase in Φ_{DP} values at the cloud top (left panel in Fig. 7) at altitudes of 12–15 km. The case was observed with S-band radar. Propagation effects should not significantly contribute to this increase because of not sufficient propagation path in the cloud. The increase in Φ_{DP} is about 5° . Areas slightly below this increase have lower Φ_{DP} values although the propagation paths for that area are longer and the paths go through more strong echoes. These features allow concluding that increase in δ in the upper area is about 5° .

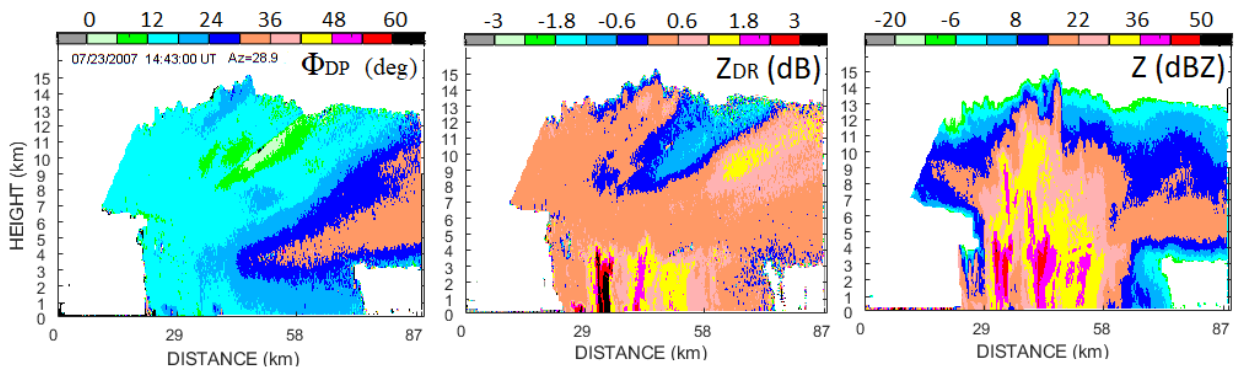


Fig. 7. Differential phase (left), differential reflectivity (center), and reflectivity (right) fields collected with KOUN on 23 July 2007 at 1443 UTC at an azimuth of 28.9° .

In the same image one can see an area of negative Φ_{DP} at heights of 9-12 km, where a drop in Φ_{DP} reaches 16° . This area coincides with negative Z_{DR} values (central panel in Fig. 7) that indicates the presence of ice particles oriented primarily vertically. Note that this area is limited in range along radials that indicates negative δ . By excluding possible propagation contribution to Φ_{DP} , the estimation of negative δ is -6° .

In ice clouds, δ values depend on crystal habits and their orientation. In the absence of strong electric fields, ice particles fall down with their maximal dimensions being horizontally oriented in the mean. In such cases, an increase in δ values is typically 2-3° (Fig. 8, see the upper part of the clouds at horizontal distances beyond 20 km). Values of large Z_{DR} values in clouds frequently have a form of localized areas (central panel in Fig. 8).

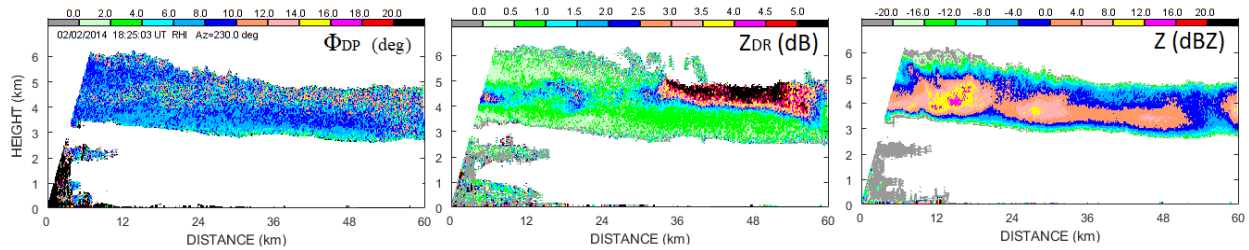


Fig. 8. Same layout as in Fig. 7. The data were collected 2 February, 2014 at 1825 UTC at an azimuth of 230° .

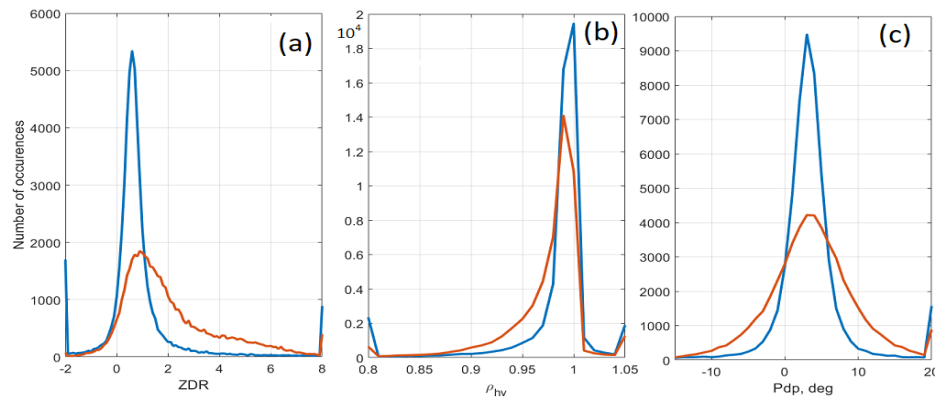


Fig. 9. (a): Distributions Z_{DR} values from heights 3-4 km (blue) and 5-6 km (brown) from a case shown in Fig. 8. (b) and (c): Same as in (a) but for ρ_{hv} and Φ_{DP} respectively.

Distributions of Z_{DR} , ρ_{hv} , and Φ_{DP} in the cloud are shown in Fig. 9. The distributions for cloud areas at heights 3-4 km are shown with the blue lines and the red curves correspond to the heights 4-5 km. The mean ρ_{hv} in the lower and upper cloud areas are 0.982 and 0.978, respectively, and the median Φ_{DP} are 3.1° and 5.4° . The propagation contribution to Φ_{DP} can be neglected for the cloud so that the difference in δ in the lower and upper areas is 2.4° in the mean. The Φ_{DP} distribution for the upper cloud area (the red curve) is wider than that for the lower area (the blue curve) because the ρ_{hv} values in the upper area are lower than those in the lower area.

The above results are valid for particles at fixed orientations in thunderstorms. If strong electric fields are absent in clouds, ice particles flutter in the air and fall with their larger dimension to be horizontal in the mean. Fluttering particles produce lower Z_{DR} and δ values. Values of δ are calculated from the correlation function R_{hv} (Melnikov 2017)

$$R_{hv} = e^{j\psi_{sys} + j\Phi_{DP}} [\langle |\alpha_a|^2 \rangle + \text{Re}(\langle \alpha_a^* \Delta \alpha \rangle) C_4 + j \text{Im}(\langle \alpha_a^* \Delta \alpha \rangle) C_5 + (\langle |\Delta \alpha|^2 \rangle) C_6], \quad (16)$$

where ψ_{sys} is the system differential phase ($\psi_{sys} = \psi_t + \psi_r$), Φ_{DP} is the propagation differential phase, and C_4 , C_5 , and C_6 are functions of ψ_t and σ_θ . The latter parameter is the standard deviation in canting angle of fluttering particles. Variable δ is obtained as

$$\delta = \arg(R_{hv}) - \psi_{sys} - \Phi_{DP}. \quad (17)$$

Fig. 10 presents results of calculated values of ρ_{hv} and δ for Rayleigh ice plate scatterers fluttering in the air. The standard deviation of the canting angles are 15° , which is the value obtained by Garrett et al. (2015) and Melnikov 2017. Panels (a) and (b) present results for a very thin ice plate. At phase $\psi_t = 0^\circ$, the δ values are very close to 0° . The maximal δ of 7° is attained at $\psi_t = 90^\circ$ at horizontal incidence. Note also that δ is not equal to 0° at vertical incidence for non-zero ψ_t . This is because non-symmetric dual-polarization wave destroy scattering symmetry at vertical incidence. The same variables are shown in Figs 10(c, d), but for an ice plate having the axis ratio (b/a in Fig. 1) of 0.3. The ρ_{hv} values are much higher than for the very thin plates and the δ values drop to about 2° maximum. Note that such δ values are observed in the case in Fig. 8.

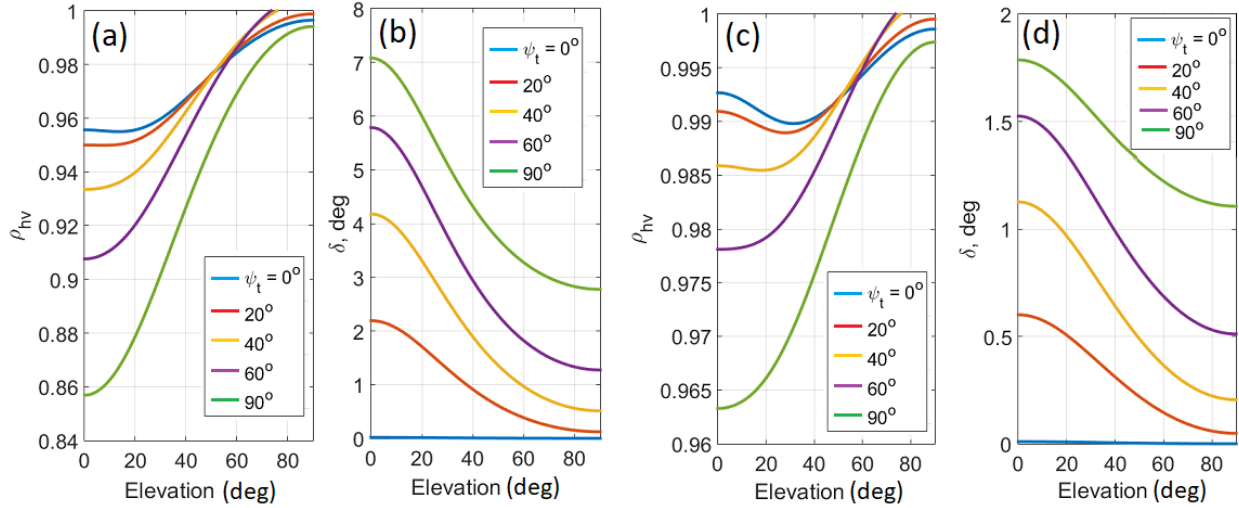


Fig. 10. (a) and (b): Values of ρ_{hv} and δ , respectively, for very thin ice plates as functions of the antenna elevation angle and for indicated phase ψ_t . The standard deviation of the canting angles is 15° . (c) and (d): Same as in (a) and (b), but for an axis ratio (b/a) of 0.3.

Three conclusions can be drawn from the presented results. 1) Values of δ can be used as a property parameter of ice particles. Values of δ of a few to several degrees are measurable. 2) To use δ values, the differential phase ψ_t between incident orthogonal waves should be known (measured). Phase ψ_t affects measured δ strongly. 3) Measured δ can be used for constraining the retrieval of parameters of ice cloud particles. Values of δ measured with SHV and AHV radars can be quite different.

3. Ice particles in the melting layer

The polarimetric properties of particles in the melting layer are characterized with increases of the Z_{DR} and Φ_{DP} values and decreases of the ρ_{hv} values in comparisons with the variables in cloud areas above and below the melting layer. An increase in Z_{DR} can reach 5 dB (for instance, in case in Fig. 12) and increase in Φ_{DP} can exceed 10° (e.g., Griffin et al. 2019). Values of ρ_{hv} can be as low as 0.7. Fig. 11 presents a vertical cross section collected with KOUN on June 15, 2015. The increase in Φ_{DP} with subtracting the propagation phase is about 2.3° and the increase in Z_{DR} is 1.6 dB. The ρ_{hv} values drop to 0.86. In case in Fig. 12, these parameters are 2.5° , 4.7 dB, and 0.822.

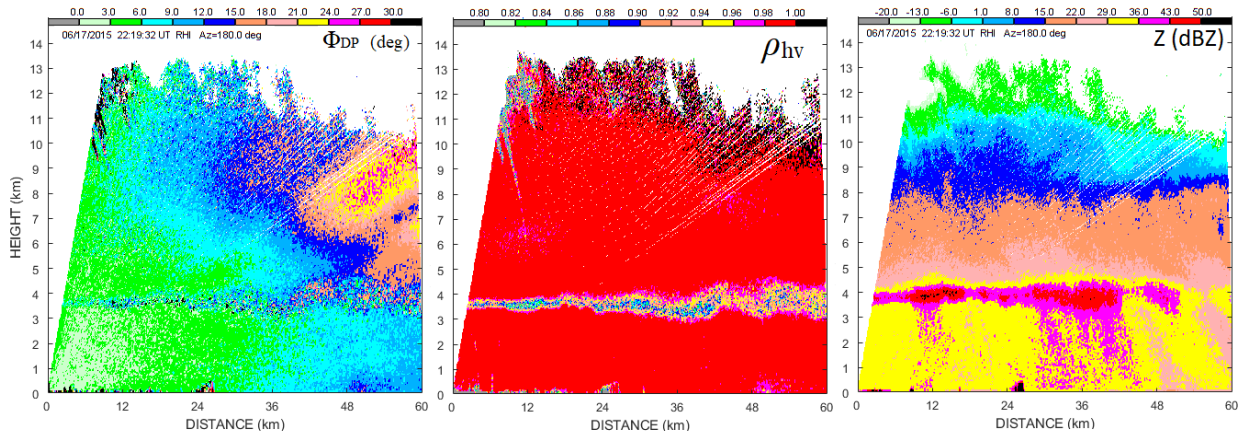


Fig. 11. Vertical cross section of Φ_{DP} , ρ_{hv} , and Z fields observed with KOUN on June 17, 2015 at 2219 UTC at an azimuth of 180° .

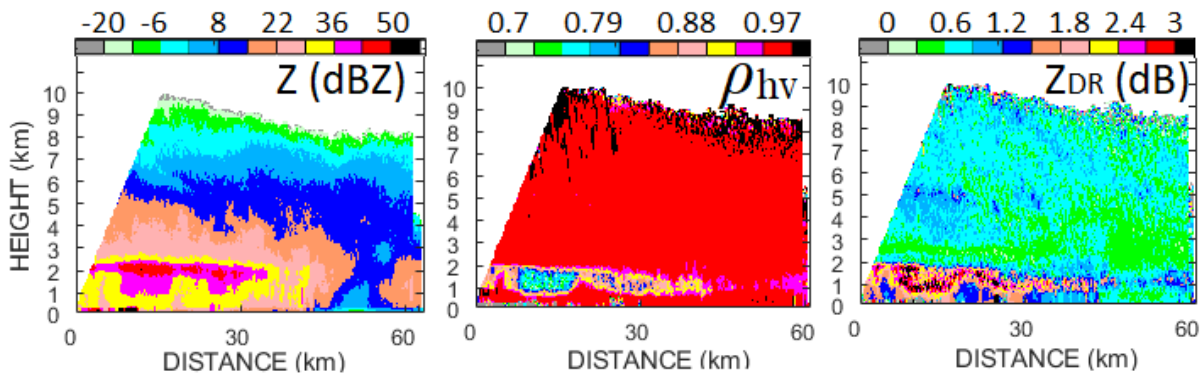


Fig. 12. Vertical cross section of Z , ρ_{hv} , and Z_{DR} fields observed with KOUN on March 26, 2014 at 1556 UTC at an azimuth of 230° .

The large intervals in the dual-polarization variables point to large variations in shapes and water content in ice particles in the melting layer that makes modeling of melting particles challenging. Ice particles just above the melting layer have been represented as a mixture of ice and air at various proportions or as a

collection of ice needles (Klaassen 1988, Fabry and Zawadzki 1995, Fabry and Szyrmer 1999, Zawadzki and Szyrmer 1999). In the case of little ice volume content in particles, Z_{DR} values above the melting layer drop and can reach 0.1- 0.3 dB. Observations with KOUN show that this scenario is not the only the case and high Z_{DR} above the melting layer has also been observed that indicates the presence of plate-like ice particles. Fragments of broken dendrites are also observed in the melting layer that can increase Z_{DR} values.

The processes in the melting layer are complicated and poorly understood. A mixture of ice and water in a particle results from various processes. Variety of ice particles' shapes lead to various scenarios of melting. On the other hand, completely melted droplets are present in the layer and can collide with ice particles. Various processes lead to different proportions of ice and water in particles. Some results for ice plates and dendrites containing water are shown in this section.

Water on/in ice particles significantly increases dielectric permittivity of the scatterers. There are two approaches in the calculations of dielectric properties of melting ice particles. 1) Scatterers consist of a uniform mixture of ice and water (the Maxwell-Garnet equation). 2) An ice particle is covered with a water film (the Boren-Huffman equation). Melting particles flutter in the air that impacts radar variables. The flutter intensity is characterized with the standard deviation σ_θ of their canting angle θ . It is assumed in this section that angle φ (Fig. 1) is uniformly distributed.

Fig. 13 presents Z_{DR} and δ for melting ice plates and needles with a water volume fraction of 20% and $\sigma_\theta = 25^\circ$; Z_{DR} and δ are shown as functions of antenna elevation angle. The Maxwell-Garnet equation has been used to calculate the dielectric properties. Water was the matrix and ice is inclusion (Meneghini and Liao, 2000). Z_{DR} does not depend on phase in transmit ψ_t (Fig. 13a) and is almost the same for plates and needles. Phase δ increases with ψ_t from 0° to $50..55^\circ$ and then decreases (Fig. 13b). Phase δ is 0° for $\psi_t = 0^\circ$. It follows from Fig. 13b that additional information about scattering particles can be obtained if radar is capable of changing ψ_t .

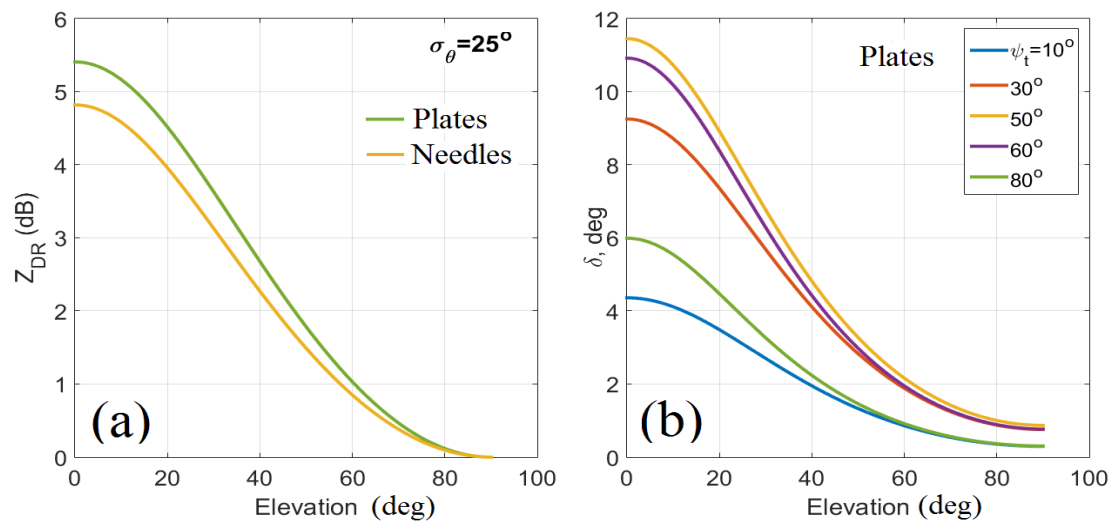


Fig. 13. Z_{DR} and δ for ice particles consisting of 80% of ice and 20% of water in their volumes. The standard deviation in the particles' canting angles is 25° . Phase in transmit ψ_t varies from 10° to 80° .

Ice particles can collide with water drops in the melting layer. After the collision, an ice particle could be completely covered with a water film. In such a model, the scattering properties can be calculated using equations from Boren and Huffman (1986). Fig 14 presents Z_{DR} and δ for thin ice plates covered with a water film of a thickness of $0.02a$, where a is the largest size of the particle. The standard deviation in the particles' canting angles is 25° . Fig. 14 demonstrates that very thin water coat strongly affects Z_{DR} and δ . The incident differential phase ψ_t plays a significant role in the value of phase δ .

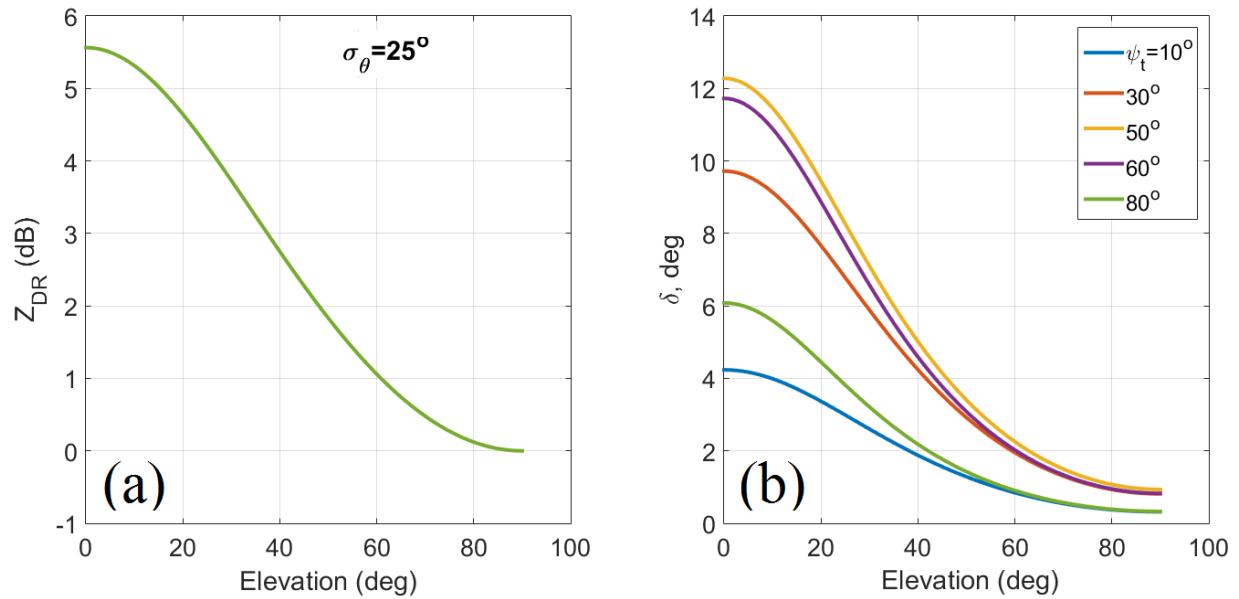


Fig. 14. Z_{DR} and δ for thin ice plates covered with a water film of a thickness of 0.02 of the a -size. The standard deviation in the particles' canting angles is 25° . Phase in transmit ψ_t varies from 10° to 80° .

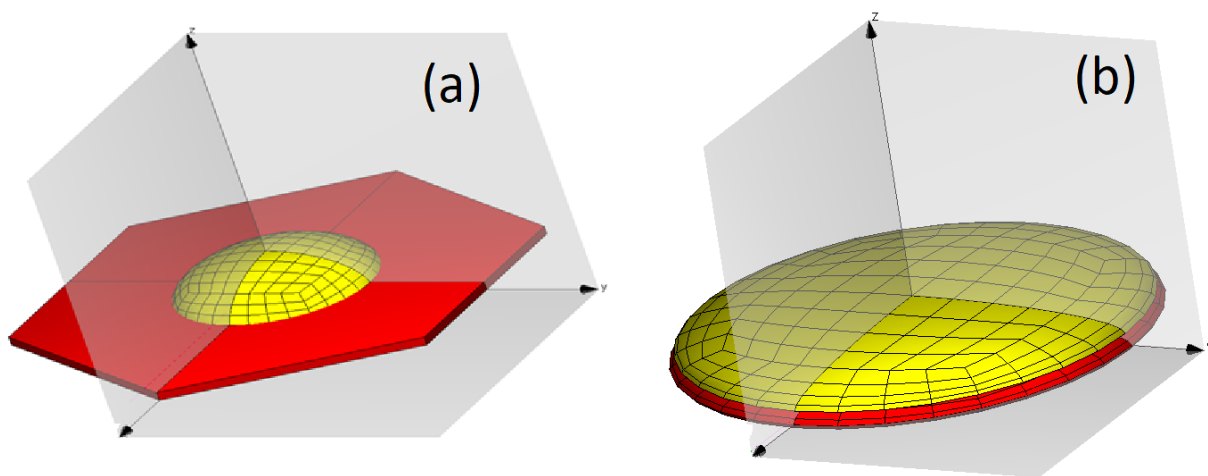


Fig. 15. Model of ice particles (in red) with a water drop (in yellow) on them. (a): A small water droplet covers a small portion of the ice particle. (b): the water film covers the whole top of the ice particle.

One more model has been considered in this study: an ice particle with a water film on its top (Fig. 15a). In panel (a), the water droplet has a form of a cap. In panel (b), water covers the whole top of the ice particle.

Results of the calculations are shown in Figs. 16 and 17 generated at the following parameters (the a/b values are exaggerated in Fig. 15 for better viewing):

Panel in Fig. 15	Diameter of ice particle	Axis ratio of the ice particle	Diameter of water patch	Axis ratio of water drop
(a)	5 mm	0.1	1 mm	0.3
(b)	1 mm	0.1	1 mm	0.05

Results of the calculations are shown in Fig. 16 (corresponds to the model in Fig. 15a) and Fig. 11 (corresponds to the model in Fig. 15b). The mean orientation of the particles is horizontal. The standard deviation in the canting angles is 30° . One can see that Z_{DR} for the models are about the same, but phases δ differ significantly. The maximal δ for model in Fig. 15b is about 11° (at an antenna elevation angle of 0°).

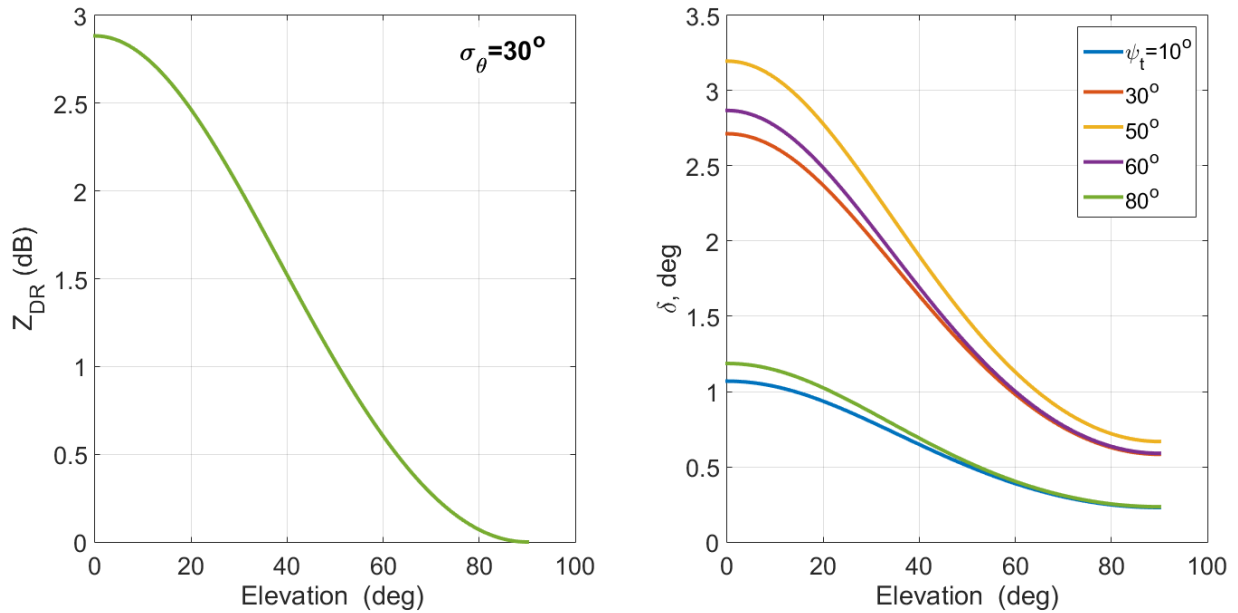


Fig. 16. Same as in Fig. 13, but for the model particle shown in Fig. 15a.

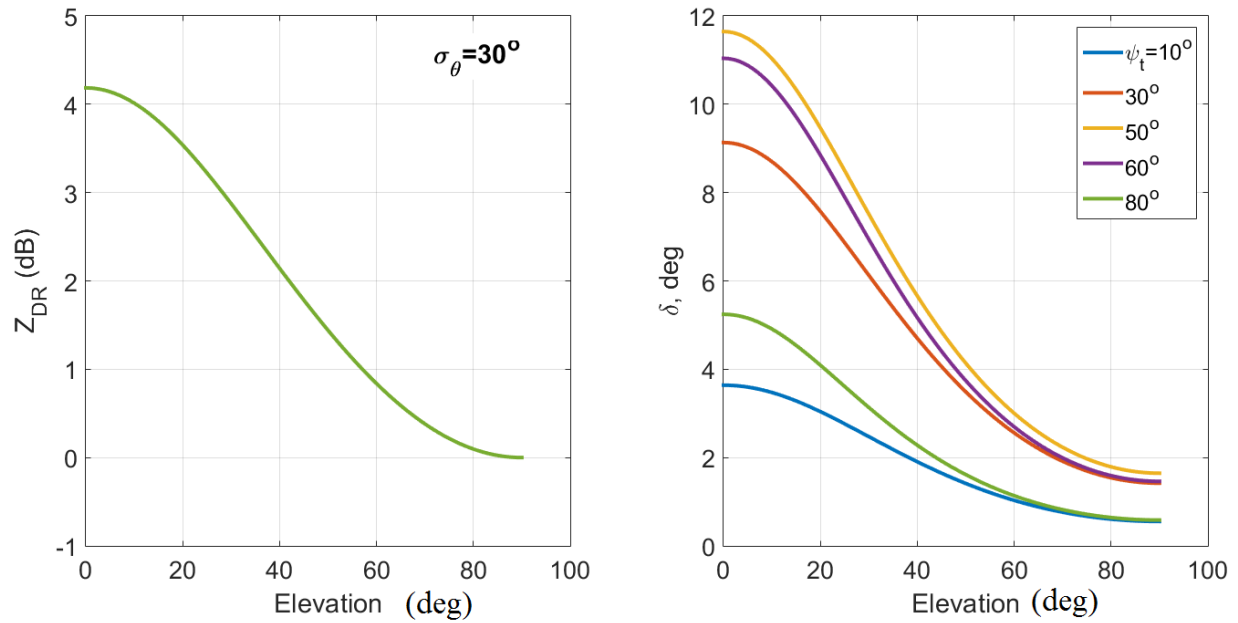


Fig. 17. Same as in Fig. 16, but for the model particle shown in Fig. 15b.

Ice particles falling through the melting layer melt and/or collide with water drops and acquire water on their surfaces. A model particle in a form of a dendrite (red) has a water drop (blue) in its center (Fig, 18). The size of the crystal is 10 mm. The thickness of the crystal is 0.4 mm. The diameter of the drop is 2 mm and its oblateness is 0.3 on the crystal. The green arrow in the figure shows the direction of incident radiation and the red arrow shows polarization of the wave, vertical in this case.

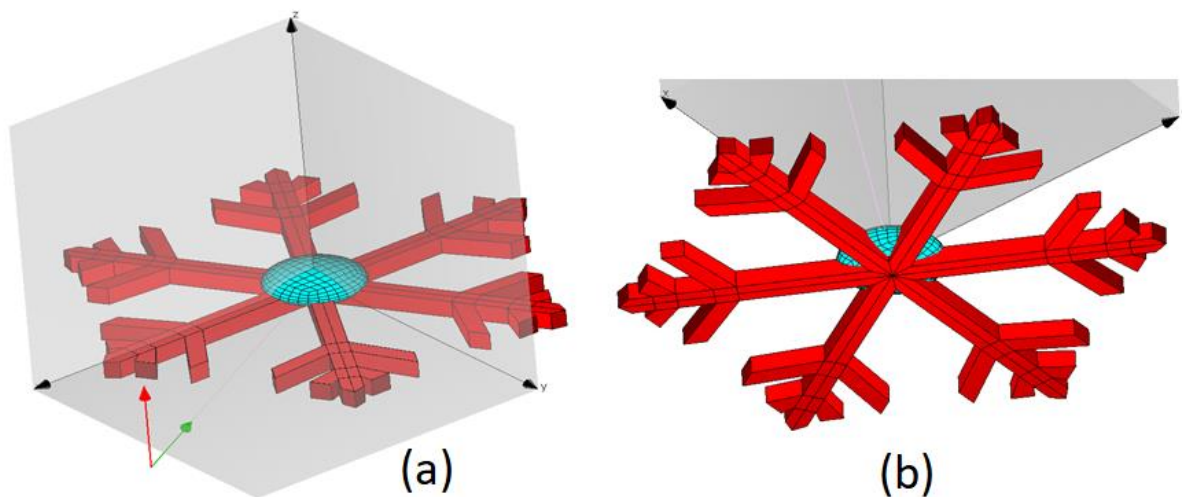


Fig. 18. Ice dendrite (in red) of 10 mm long and a water drop (in blue) of 2mm in diameter and oblateness of 0.3. (b): Same model particle as in Fig. 18a, but viewed from the bottom.

To get some sense about radar variables from such particles, Z_{DR} and δ have been calculated as functions of the incident angle θ (Fig. 1). The crystal is oriented horizontally. Fig. 19 shows Z_{DR} and δ for the particle in Fig. 18 (Dendr+Drop in the figure legend, the red line) and dendrite alone (the blue line). One can see that the main contributions to Z_{DR} and δ come from the water drop. No flutter was introduced.

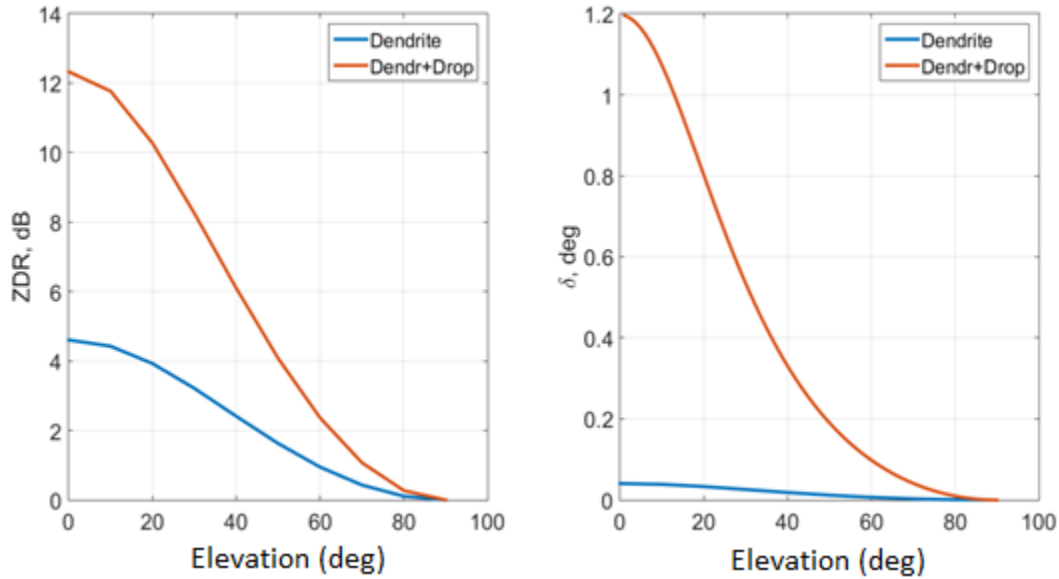


Fig. 19. Z_{DR} (left) and δ (right) as functions of the incidence angle θ for dendrite + drop (the bred curves) and dendrite alone (in blue). The particle is oriented horizontally.

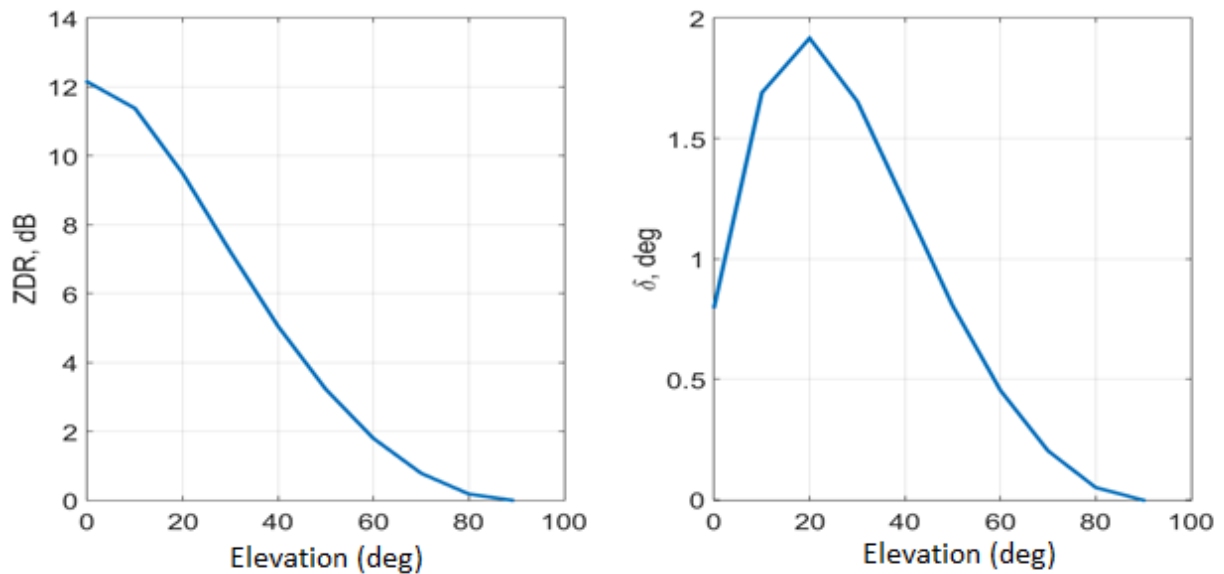


Fig. 20. Z_{DR} and δ as functions of the incidence angle θ for the model shown in Fig. 14. Differential phase in transmit is 0° . Horizontally oriented particle.

One more model studied with WIPL is shown in Fig. 15a. A hexagonal ice prism (in red) has a water droplet on it. The size of the plate is 5 mm and its thickness is 0.1 mm. The droplet is modeled as half of a spheroid with the diameter of 4 mm and an axis ratio height/radius of 0.5. Z_{DR} strongly depends on the incidence angle (Fig. 20 left). Phase δ is small (Fig. 20 right) for the differential phase in transmit of 0° . The Z_{DR} values drop significantly for fluttering particles (Fig. 21, left) and δ values increase substantially (Fig. 21 right) at nonzero ψ_t . So fluttering can significantly impact Z_{DR} and δ values.

The considered water inclusions do not change the center of mass of the particles because the water droplets covered the center of particles. Most likely, such situations occur not frequently. Collisions of ice crystals with droplets most likely create asymmetric particles with the center of mass not at the centers of ice crystals (for instance, Fig. 22). In such cases, the mean orientation of the particles is not horizontal. Ice crystals with water inclusions may exhibit much larger δ than those for the crystals alone.

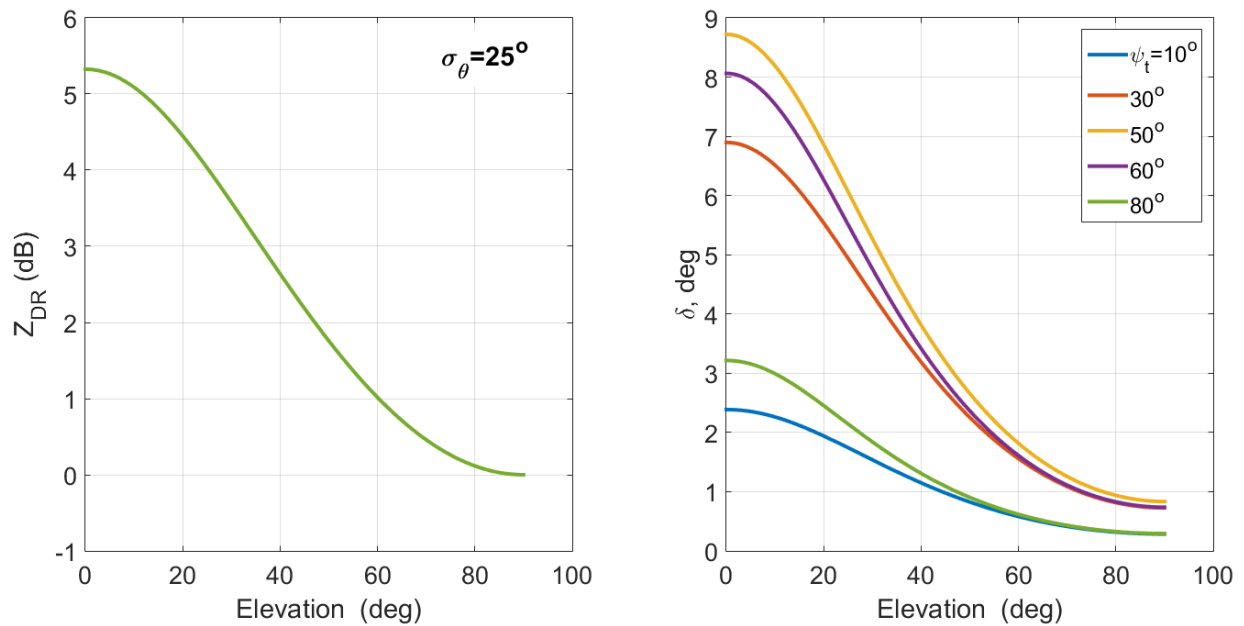


Fig. 21. Same as in Fig. 16, but for the model particle shown in Fig. 15a. The standard deviation in the canting angle is 25° .

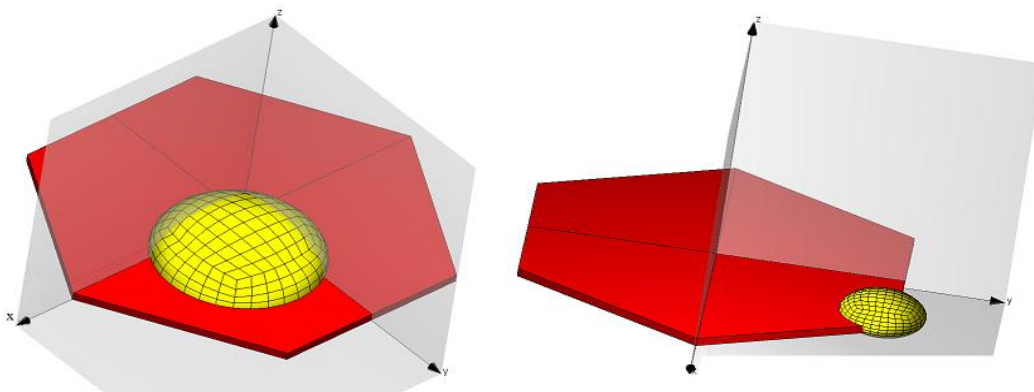


Fig. 22. Same as in Fig. 15a, but the centers of droplets (in yellow) are shifted from the center of the crystal (in red).

4. Hail

Various polarization properties are observed in hail thunderstorms. The Z_{DR} values from hail at S band span an interval from -3 to 6 dB. The negative Z_{DR} values can be caused by large non-spherical hailstones of resonance sizes and large positive Z_{DR} could be caused by a toroidal water film on the surface of a melting hailstone. Values of ρ_{hv} typically are lower in hail cores relative to surrounding areas and the δ phases can exceed dozen degrees. In hail thunderstorm in Fig. 23, Z_{DR} reaches 6 dB and δ is about 16° in the hail core.

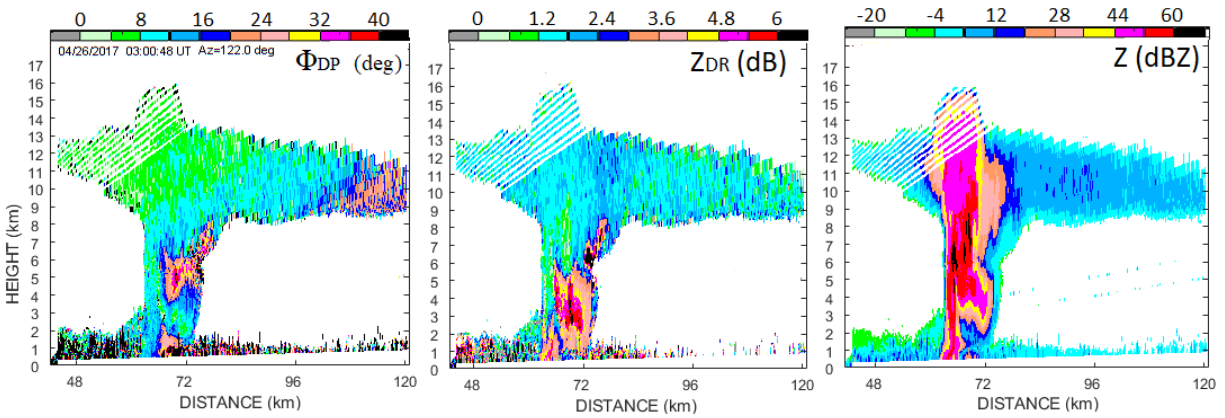


Fig. 23. Vertical cross section of Φ_{DP} (left), Z_{DR} (center), and Z (right) fields observed with KOUN 26 April, 2017 at 0300 UTC in an azimuth of 122° .

Two features are discussed in this section: 1) Possible impacts of ψ_t on measured ρ_{hv} in hail cores. Values of ρ_{hv} do not depend on attenuation and is convenient for comparisons of data collected with various radars. 2) Possible impact of the phase ψ_t on observed δ .

Three WSR-88D radars are located at Norman, OK. Radar images of hail producing thunderstorm observed 31 May, 2013 at an antenna elevation of 0.5° are shown in Fig. 24. The storm produced EF3 tornado at the time. The tornadic area was surrounded with an arc of high reflectivity to the North from the tornado vortex indicated with an arrow in the top left panel of Fig. 24. This arc indicated with "1" in that panel and is seen along the inflow edge of the storm. This feature are typical in tornadic storms (e.g., Schwarz and Burgess 2011) and can be seen in images from the three radars in Fig. 24.

No hail reports were issued in area "1" of strong reflectivity. Large hail with sizes up to 6 cm was produced by the ridge of high reflectivity indicated with "2" in the left top panel of Fig. 24. Maximal reflectivity values from areas "1" and "2" were 63-67 dBZ, i.e., about the same. To compare radar polarimetric characteristics from the areas, values of ρ_{hv} have been analyzed as a function of reflectivity for the reflectivity values larger than 40 dBZ. This threshold have been chosen because probability of hail increases sharply for reflectivity values exceeding 50 dB (Witt et al. 1994).

Figs. 25 presents the mean ρ_{hv} as a function of reflectivity for areas "1" and "2", where the mean values are indicated with the brackets, i.e., $\langle \rho_{hv} \rangle$. Values of $\langle \rho_{hv} \rangle$ as function of Z from the three radars exhibit different behaviors: the $\langle \rho_{hv} \rangle$ values from three radars are about the same in area "1" up to Z of 57 dB, but are different for area "2" for $Z > 50$ dBZ. Values of $\langle \rho_{hv} \rangle$ from KOUN increase with Z whereas $\langle \rho_{hv} \rangle$ from KTLX and KCRI drop at $Z > 50$ dB.

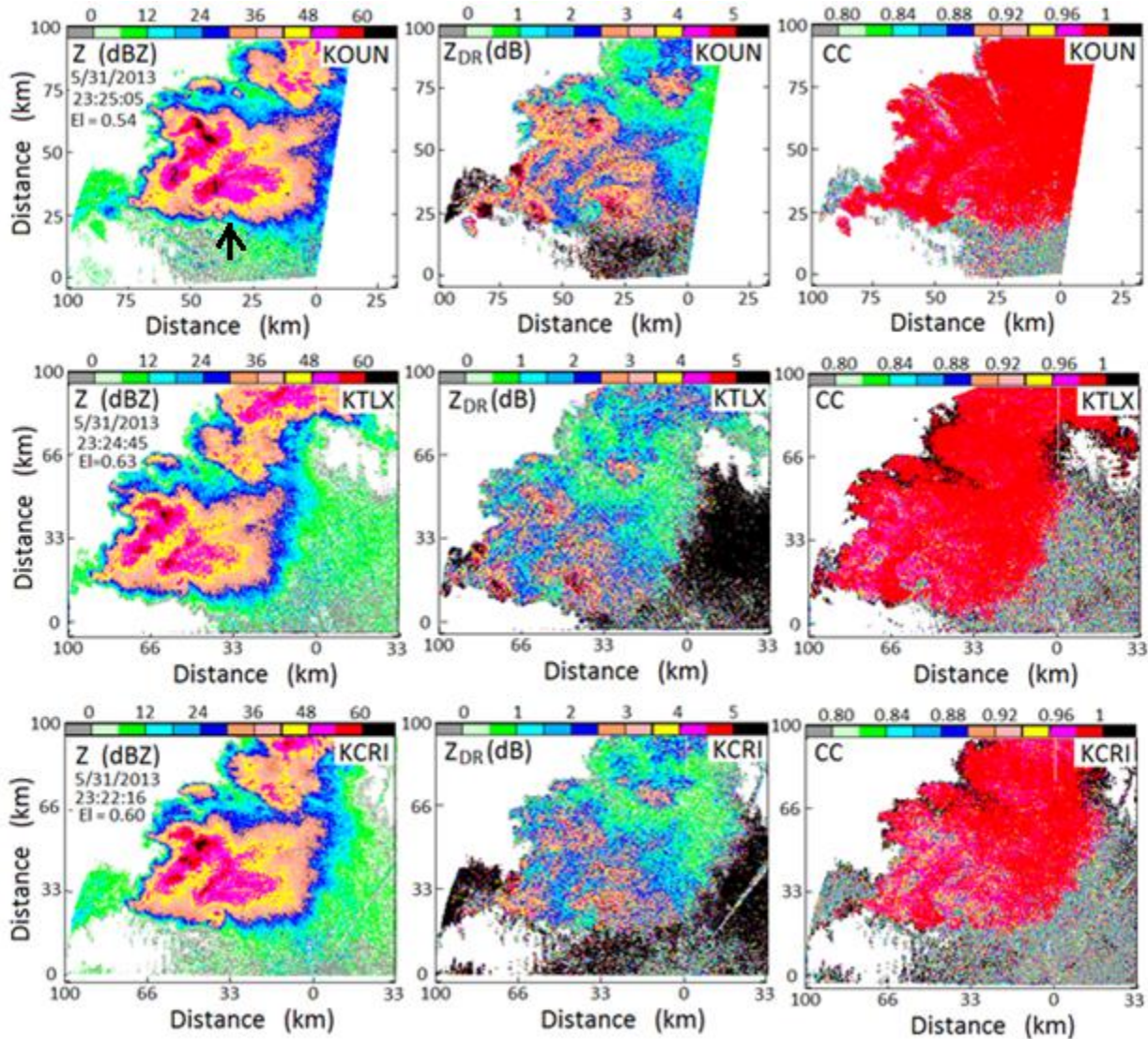


Fig. 24. Polarimetric fields on May 31, 2013 at about 23:24 UTC. The data were collected with KOUN, KTLX, and KCRI; the radar names are indicated in the right top angles in each panel. CC stands for correlation coefficient. The area with a tornado is shown in the left top panel with a vertical arrow.

Adjacent WSR-88Ds operate at slightly different frequencies to reduce interference signals. Hailstones in area “2” are not small compared to the radar wavelength therefore radar characteristics of hail exhibit resonant features even inside the S band. So one of radar parameters that impact the polarization properties is radar frequency. Another radar parameter is the differential phase in transmit ψ_t .

Large hailstones frequently have nonspherical shapes that means they do not tumble randomly in the air. To acquire nonspherical shapes, hailstones must precess in the air. Such precessing can lead to positive Z_{DR} which are observed in hail cores frequently. Precessing affects the differential phase upon scattering and correlation coefficient. To study a possible impact of ψ_t on ρ_{hv} and δ , a hailstone have been modeled as a wet prolate spheroid with an axis ratio of 0.7. The water film on the hailstone’s surface has been obtained from the results of Rasmussen and Heimsfield (1987). The standard deviation of the tumbling

hailstone has been set to 30° and the mean canting angle of the tumbling hailstone has been assumed to be 0° .

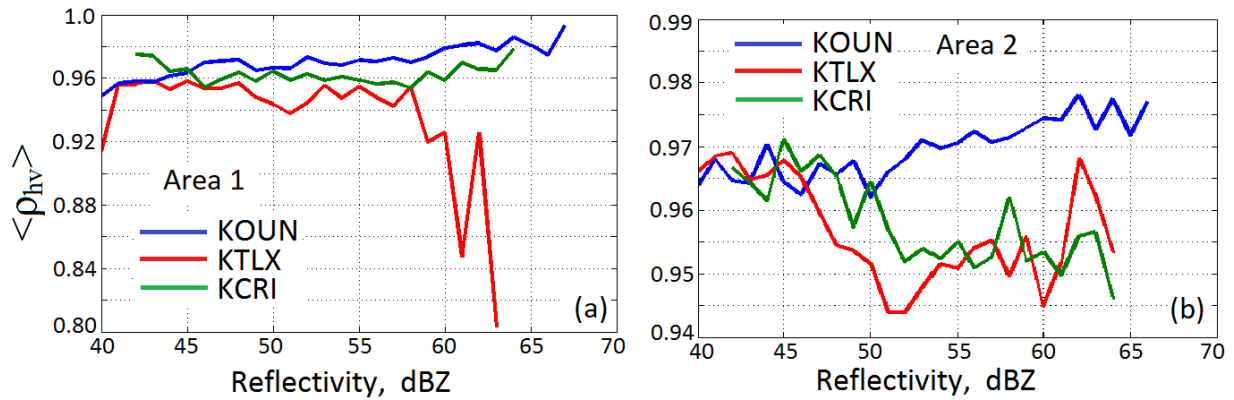


Fig. 25 (a): The mean correlation coefficients as functions of reflectivity for area “1” of high reflectivity. (b): Same as in (a) but for area “2”.

The values of $\langle \rho_{hv} \rangle$ from KOUN and KCRI in area “2” drop by 0.02 at $Z > 50$ dB from KTLX’s data (Fig. 25b). Theoretical dependences of ρ_{hv} on hail size and ψ_t are shown in Fig. 26b. One can see that ρ_{hv} can differ by 0.02 for various ψ_t at the hail size larger than 4 cm that is in the range of observed hail sizes on the ground. So different ψ_t on two radars can lead to different ρ_{hv} values in hail cores observed with those radars.

Fig. 26a presents dependences of phase δ as a function of the hail size and ψ_t . The same properties of hailstones have been used to generate the figure. It is seen that the phase δ remains small up to a hail size of 3 cm and beyond that the δ values increase with the hail size. Thus, the phase δ has a potential in hail sizing and the phase ψ_t does not affect this dependence much.

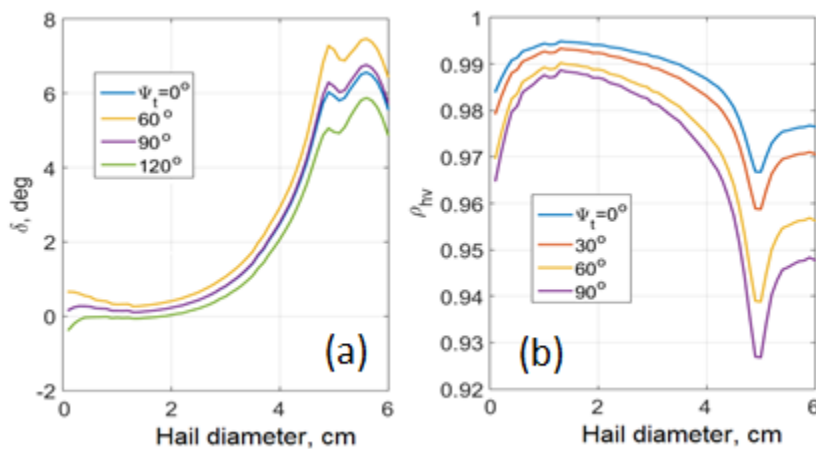


Fig. 26. Phase δ and ρ_{hv} as functions of the diameter of wet hailstones at various ψ_t and for horizontal sensing. The axis ratio of the wet hailstones is 0.7. The standard deviation in the canting angles is 30° .

6. Summary

The intrinsic Z_{DR} , ρ_{hv} , and δ values are measured with radars employing alternate polarizations (AHV radar design) whereas the vast majority of weather radars employ simultaneous transmission and reception of orthogonally polarized waves (SHV design). In the SHV radars, the transmitted waves are typically shifted in phase; this phase (ψ_t) affects measured polarimetric variables. Z_{DR} , ρ_{hv} , and δ values measured with AHV and SHV radars are different. This difference is due to depolarization of waves upon scattering and vector summation of the primary and depolarized waves.

Maximal Z_{DR} values from ice plates measured with AHV radar is 10 dB, whereas for SHV radar it is 12.5 dB. Values of δ from ice cloud particles measured with AHV radar are negligible, whereas for SHV radar, maximal δ is 62.3° (section 2). For ice particles of moderate axis ratio, δ can reach 20° . Non-zero δ values from ice clouds can be only measured with SHV radar. The values of δ depend on the transmit phase ψ_t . The δ values can be positive and negative depending on orientation of particles and the system phase in transmit ψ_t . The δ -values can be used as an additional variable from scatterers if the phase ψ_t is known (measured).

Ice particles in shapes of ellipsoids and hexagonal prisms of the same axis ratios (b/a) produce different Z_{DR} and δ at $b/a > 0.1$ that should be considered in retrieving the particles' parameters from radar data.

The impacts of ψ_t on measured polarization variables can explain large intervals in Z_{DR} , ρ_{hv} , and δ values observed in the melting layer. It was shown in section 3 that these values can be produced by Rayleigh scatterers and there is no need to assume the presence of large scatterers with resonance sizes in the melting layer. The polarization properties of melting ice particles can be modeled with the WIPL software package (section 3), which features various capabilities in composing of ice and water in a particle.

Section 5 presents some arguments on the interpretation of different ρ_{hv} values observed with three WSR-88Ds radars in hail cores. Hail cores are frequently located inside thunderstorms and radar waves experience strong attenuation in sensing hail cores. Reflectivity and Z_{DR} are typically compromised by attenuation. In contrast, ρ_{hv} values are immune to attenuation and, therefore, can be compared without applying any attenuation correction techniques. Such a comparison (section 5) shows that the mean ρ_{hv} values from three WSR-88Ds observed in a hail core are different that can be a result of two reasons: 1) different radar frequency and 2) different system differential phases in transmit ψ_t . It was shown that ψ_t affects ρ_{hv} values (Fig. 26b). Fig. 26a demonstrates that the δ -values (immune to attenuation) from hail cores increase rapidly for hailstone sizes larger than 3 cm that can be used in the identification of large hail.

Dependences of Z_{DR} , ρ_{hv} , and δ values on the radar system differential phase upon transmission ψ_t point to additional measurement opportunities. Switching ψ_t during the radar dwell time can deliver additional information on scatterers. Fast switching can be available on phased array radars for which switching of ψ_t can be done from pulse to pulse. Such fast switching of ψ_t is quite challenging for traditional weather radars.

References

- Bader M.J., S.A. Clough, G.P. Cox, 1987: Aircraft and dual polarization radar observations of hydrometeors in light stratiform precipitation. *Q.J.R. Meteorol. Soc.*, **113**, 491 – 515.
Bohren, C.F., and D.R. Huffman, 1983: *Absorption and Scattering of Light by Small Particles*, John

- Whilley and Son, San Diego, CA.
- Bringi, V. N., and V. Chandrasekar, 2001: *Polarimetric Doppler Weather Radar. Principles and Applications*. Cambridge University Press. 636 pp.
- Caylor, I. J., and V. Chandrasekar, 1996: Time-varying crystal orientation in thunderstorms observed with multiparameter radar. *IEEE Trans. Geosci. Remote Sens.*, **34**, 847–858.
- Doviak, R. J. and D. S. Zrnic, 2006: *Doppler radar and weather observations*, 2nd ed., Academic Press, 562 pp.
- Fabry, F., and I. Zawadzki, 1995: Long-term radar observations of the melting layer of precipitation and their interpretation. *J. Atmos. Sci.*, **52**, 838–851
- Fabry, F., and W. Szyrmer, 1999: Modeling of the melting layer. Part II: Electromagnetic. *J. Atmos. Sci.*, **56**, 3593–3600.
- Garrett, T.J., S.E. Yuter, C. Fallgatter, K. Shkurko, S.R. Rhodes, and J.L. Endries, 2015: Orientation and aspect ratios of falling snow. *Geophys. Res. Lett.*, **42**, 4617-4622, doi:10.1002/2015GL064040.
- Griffin, E., T. Schuur, and A. Ryzhkov, 2018: A Polarimetric Analysis of Ice Microphysical Processes in Snow, Using Quasi-Vertical Profiles. *J. Applied Meteorol. Climat.* **57**, 31 - 50.
- Griffin, E., T. Schuur, and A. Ryzhkov, 2019: A Polarimetric Radar Analysis of Ice Microphysical Processes in Melting Layers of Winter Storms using S-band Quasi-Vertical Profiles. *J. Applied Meteorol. Climat.* In Press.
- Gossard, E.E., and R.G. Strauch, 1983: *Radar Observations of Clear Air and Clouds*. Elsevier, 280 pp.
- Hall, M.P. M., J.W. Goddard, S. M. Cherry, 1984: Identification of hydrometeors and other targets by dual-polarization radar. *Radio Sci.*, **19**, 132-140.
- Hendry, A., and G. C. McCormick, 1976: Radar observations of alignment of precipitation particles by electrostatic fields in thunderstorms. *J. Geophys. Res.*, **81**, 5353–5357.
- Hogan, R. J, P.R Field, A.J. Illingworth, A.J. Cotton, T.W. Chouarton, 2002: Properties of embedded convection in warm-frontal mixed-phase cloud from aircraft and polarimetric radar. *Q.J.R. Meteorol. Soc.*, **128**, 451-476.
- Hogan, R.J., L. Tian, P.R.A. Brown, C. D. Westbrook, A.J. Heymsfield, and J.D. Eastment, 2012: Radar scattering from ice aggregates using the horizontally aligned oblate spheroid approximation. *J. Applied Meteorol. Climat.*, **51**, 655-671.
- Holt, A.R., 1984: Some factors affecting the remote sensing of rain by polarization diversity radar in 3- to 35-GHz frequency range. *Radio Sci.*, **47**, 1399–1421.
- Hubbert, J. C., S. M. Ellis, W.-Y. Chang, S. Rutledge, M. Dixon, 2014a: Modeling and interpretation of S-band ice crystal depolarization signatures from data obtained by simultaneously transmitting horizontally and vertically polarized fields. *J. Applied Meteorol. Climat.* **53**, 1659 – 1677.
- Hubbert, J. C., S. M. Ellis, and W.-Y. Chang, Y.-C. Liou, 2014b: X-Band polarimetric observations of cross coupling in the ice phase of convective storms in Taiwan. *J. Applied Meteorol. Climat.* **53**, 1678 – 1695.
- Klaassen, W., 1988: Radar observations and simulation of the melting layer of precipitation. *J. Atmos. Sci.*, **45**, 3741–3753.
- Matrosov, S. Y. 2015: Evaluations of the spheroidal particle model for describing cloud radar depolarization ratios of ice hydrometeors. *J. Atmos. Oceanic Technol.*, **32**, 865–879.
- Melnikov, A., V. Melnikov, and A. V. Ryzhkov, 2005: On the differential phase in the melting layer. 33rd Conference on Radar Meteorol., Albuquerque, NM, AMS.
- Melnikov, A., 2012: Differential phase upon scattering by Rayleigh particles. 7th European Conference on Radar in Meteorology and Hydrology, Toulouse, France.

- Melnikov, V., D. Zrnica, D. Burgess, and E. Mansell, 2014: Observations of hail cores of tornadic thunderstorms with three polarimetric radars. *94th AMS Annual Meeting*, Atlanta, GA. <https://ams.confex.com/ams/94Annual/webprogram/Paper233038.html>
- Melnikov, V., D. Zrnica, R. Rabin, and P. Zhang, 2008: Radar polarimetric signatures of fire plumes in Oklahoma. *Geophys. Res. Letters*, **35**, doi:10.1029/2008GL034311.
- Melnikov, V., D. Zrnica, and R. Rabin, 2009: Polarimetric radar properties of smoke plumes: A model. *J. Geophys. Res.*, **114**, D21204, doi:10.1029/2009JD012647.
- Melnikov, V. 2017: Axis ratios and flutter angles of cloud ice particles: retrievals from radar data. *J. Atmos. Oceanic Technol.*, **30**, 1691–1703.
- Melnikov, V. 2018, Differential phase upon transmission as a new radar parameter. ERAD-2018.
- Meneghini R. and L. Liao, 2000: Effective Dielectric Constants of Mixed-Phase Hydrometeors, *J. Atmos. Oceanic Technol.*, **17**, 628-640.
- Pruppacher, H. R., and J. D. Klett, 1997: *Microphysics of Clouds and Precipitation*. Kluwer Academic, 954 pp., 1997.
- Rasmussen, R. M., and A. J. Heymsfield, 1987: Melting and shedding of graupel and hail. Part I: Model physics. *J. Atmos. Sci.*, **44**, 2754–2763, [https://doi.org/10.1175/1520-0469\(1987\)044,2754:MASOGA.2.0.CO;2](https://doi.org/10.1175/1520-0469(1987)044,2754:MASOGA.2.0.CO;2).
- Ryzhkov, A.V., and D. S. Zrnica, 2007: Depolarization in ice crystals and its effect on radar polarimetric measurements. *J. Atmos. Oceanic Technol.*, **24**, 1256 – 1267.
- Shrom, R.S., and M. R. Kumjian 2018, Bulk-Density Representations of Branched Planar Ice Crystals: Errors in the Polarimetric Radar Variables, *J. Appl. Meteorol. Climat.*
- Szyrmer, W., and I. Zawadzki, 1999: Modeling of the melting layer. Part I: Dynamics and microphysics. *J. Atmos. Sci.*, **56**, 3573–3592.
- Schwarz, C.M. and D.W. Burgess, 2011: Supercell polarimetric signatures at X-Band: Data from VORTEX2. Extended Abstracts, *35th Conf. Radar Meteorol.*, AMS, <http://ams.confex.com/ams/35Radar/webprogram/Paper191298.html>
- Trömel, S., M. R. Kumjian, A. V. Ryzhkov, C. Simmer, and M. Diederich, 2013: Backscatter differential phase – Estimation and variability, *J. Appl. Meteorol.*, **52**, 2529-2548.
- Vivekanandan, J., W. M. Adams, and V. N. Bringi, 1991: Rigorous approach to polarimetric radar modeling of hydrometeor orientation distributions, *J. Appl. Meteorol.*, **30**, 1053–1063.
- Westbrook, C.D., A.J. Illingworth, E.J. O’Connor, R.J. Hogan, 2010: Doppler lidar measurements of oriented planar ice crystals falling from supercooled and glaciated cloud layers. *Q. J. R. Meteorol. Soc.*, **136**, 260-276.
- Westbrook, C.D., 2014: Rayleigh scattering by hexagonal ice crystals and the interpretation of dual-polarization radar measurements. *Q. J. R. Meteorol. Soc.*, **140**, 2090-2096.
- Witt, A., M. D. Eilts, G. J. Stumpf, J. T. Johnson, E. De W. Mitchell, K. W. Thomas, 1998: An Enhanced Hail Detection Algorithm for the WSR-88D. *Wea. Forecasting*, **13**, 286–303.